Functionality multiplexing in high-efficiency metasurfaces based on coherent wave interferences

Yuejiao Zhou, Tong Liu, Changhong Dai, Dongyi Wang and Lei Zhou

---

Related articles

Dynamic interactive bitwise meta-holography with ultra-high computational and display frame rates
Yuncheng Liu, Ke Xu, Xuhao Fan, Xinger Wang, Xuan Yu, Wei Xiong, Hui Gao
Opto-Electronic Advances   2024 **7**, 230108   doi: 10.29026/oea.2024.230108

All-optical controlled-NOT logic gate achieving directional asymmetric transmission based on metasurface doublet
Yijia Huang, Tianxiao Xiao, Shuai Chen, Zhengwei Xie, Jie Zheng, Jianqi Zhu, Yarong Su, Weidong Chen, Ke Liu, Mingjun Tang, Peter Müller-Buschbaum, Ling Li
Opto-Electronic Advances   2023 **6**, 220073   doi: 10.29026/oea.2023.220073

Resonantly enhanced second- and third-harmonic generation in dielectric nonlinear metasurfaces
Ji Tong Wang, Pavel Tonkaev, Kirill Koshelev, Fangxing Lai, Sergey Kruk, Qinghai Song, Yuri Kivshar, Nicolae C. Panoiu
Opto-Electronic Advances   2024 **7**, 230186   doi: 10.29026/oea.2024.230186

More related article in Opto-Electronic Journals Group website

Functionality multiplexing in high-efficiency metasurfaces based on coherent wave interferences

Yuejiao Zhou[1†], Tong Liu[2†], Changhong Dai[1], Dongyi Wang[3*] and Lei Zhou[1,4*]

Multiplexing multiple yet distinct functionalities in one single device is highly desired for modern integration optics, but conventional devices are usually of bulky sizes and/or low efficiencies. While recently proposed metasurfaces can be ultra-thin and highly efficient, functionalities multiplexed by metadevices so far are typically restricted to two, dictated by the number of independent polarization states of the incident light. Here, we propose a generic approach to design metadevices exhibiting wave-control functionalities far exceeding two, based on coherent wave interferences continuously tuned by varying the incident polarization. After designing a series of building-block metaatoms with optical properties experimentally characterized, we construct two metadevices based on the proposed strategy and experimentally demonstrate their polarization-tuned multifunctionalities at the wavelength of 1550 nm. Specifically, upon continuously modulating the incident polarization along different paths on the Poincare's sphere, we show that the first device can generate two spatially non-overlapping vortex beams with strengths continuously tuned, while the second device can generate a vectorial vortex beam carrying continuously-tuned polarization distribution and/or orbital angular momentum. Our proposed strategy significantly expands the wave-control functionalities equipped with a single optical device, which may stimulate numerous applications in integration optics.

Keywords: metasurface; coherent wave interferences; vectorial vortex beam; functionality multiplexing; orbital angular momentum; local polarization distributions; polarization-dependent

Introduction

Along with rapid developments in optical sciences and applications, there is an increasing demand on multifunctional optical devices capable of multiplexing as many as possible wave-control functionalities in one single ultra-compact system. Optical devices made by conventional dielectrics are typically bulky in sizes (compared to wavelengths). Moreover, without additional degrees of freedom to manipulate light, it is hard to

employ conventional dielectrics to realize compact optical devices with multiple functionalities, being highly unfavourable for optical integration.

Metasurfaces, ultra-thin metamaterials composed of planar subwavelength microstructures (e.g., metaatoms) possessing tailored optical responses arranged in certain pre-designed sequences, exhibit extraordinary capabilities to control light waves and thus have attracted tremendous attention recently. Through designing both metaatoms and their arranging sequences, scientists have realized various metasurfaces that can control locally scattered waves in terms of both phase and polarization, thus forming tailored light beams in the far-field based on Huygens' principle. Many fascinating wave-manipulation functionalities have been realized based on metasurfaces, such as polarization control[1–5], anomalous light deflections[6–11], propagating wave to surface wave conversion[12–15], meta-lens focusing[16–20], meta-holograms[11,21–25], etc. In particular, generation of complex optical fields including vector beams and vector vortex beams is highly desired in both fundamental science and practical applications[26–33], as the additional degrees of freedom provided by local polarization and orbital angular momentum (OAM) offer more possibilities to manipulate light properties. Moreover, employing anisotropic metaatoms with polarization-dependent scattering properties, many multifunctional metadevices have been recently demonstrated, which exhibit distinct wave-control functionalities as shined by light with different polarizations. These metadevices are typically ultra-compact, highly efficient, and exhibit diversified functionalities, all being highly desired in integration-optics applications. We note that multifunctional meta-surfaces have also been realized through varying different properties of the incident light[34–39]. However, taking only the incident polarization state as the multiplexing channel, we found that most multifunctional metadevices realized so far can only exhibit no more than two distinct wave-control functionalities, dictated by the number of independent incident polarizations[38,40–44](e.g., linear polarizations along two orthogonal directions or circular polarizations with two opposite helicities). Facing the increasing demands on functionality integrations in photonics research and applications, it is highly desired to develop new strategies for realizing metadevices with number of wave-manipulation functionalities far exceeding two.

In this paper, we propose an approach to design metadevices exhibiting (in principle) infinite number of wave-control functionalities based on coherent wave interferences tuned by continuously varying the polarization state of incident light, and experimentally verify the concept in the telecom wavelength regime (1550 nm). After designing a series of metaatoms with tailored reflection phases and polarization-conversion capabilities, we construct two functional metadevices and experimentally characterize their wave-control functionalities under illuminations of light with polarization continuously tuned along a certain path on the Poincare's sphere. Our experiments show that the first device can generate two non-overlapping yet distinct vortex beams with continuously varying strengths, while the second one can generate a single vectorial vortex beam carrying orbital angular momentum (OAM) and/or local polarization distributions (LPDs) continuously tuned by varying the incident polarization. Experimental results are in excellent agreement with numerical simulations and theoretical expectations.

Results

Concept and design strategies

We start from introducing the working principle of our proposed multifunctional metadevice, as schematically depicted in Fig. 1. Suppose that our designed metasurface can generate two distinct light beams in the far field, as shined by incident light beams possessing two orthogonal polarizations. Without losing generality, we choose left circular polarization (LCP) and right circular polarization (RCP) as two polarization bases, and assume that the reflected waves are $F_+(\boldsymbol{r})|\hat{\sigma}_+(\boldsymbol{r})\rangle$ and $F_-(\boldsymbol{r})|\hat{\sigma}_-(\boldsymbol{r})\rangle$
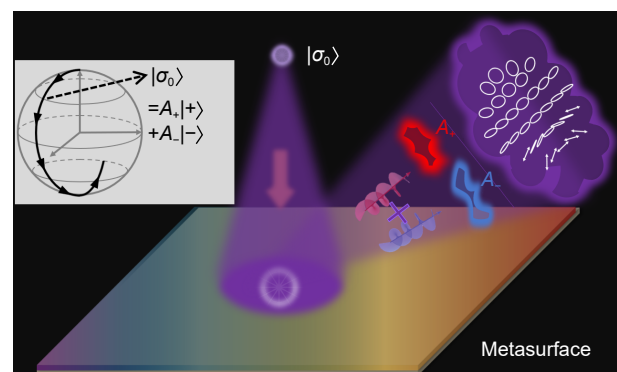
Fig. 1 | Schematics of multiplexing metadevices based on coherent wave interferences. Illuminated by a light beam with polarization continuously tuned characterized by two continuously varying circular-polarization expansion coefficients, wave reflected by the metadevice can exhibit different wave-fronts and polarization distributions dictated by two expansion coefficients.

under LCP and RCP incidences, respectively. Here, $F_{\pm}(\boldsymbol{r})$ are complex functions of $\boldsymbol{r}$ representing the non-trivial wave-fronts of two generated beams, while $|\widehat{\sigma}_{\pm}(\boldsymbol{r})\rangle$ denote the LPDs on equal-phase planes of the generated light beams. Now consider the case that the metasurface is shined by a light beam with an arbitrary polarization described by $|\sigma_0\rangle = A_+|+\rangle + A_-|-\rangle$ ($|+\rangle$ and $|-\rangle$ denote the LCP and RCP components, respectively) with A_+ and A_- being two complex amplitudes satisfying $|A_+|^2 + |A_-|^2 = 1$. Based on the law of linear decomposition, we find that the scattered light beam in this case must be $A_+ \cdot F_+(\boldsymbol{r})|\widehat{\sigma}_+(\boldsymbol{r})\rangle + A_- \cdot F_-(\boldsymbol{r})|\widehat{\sigma}_-(\boldsymbol{r})\rangle$. Obviously, the generated beams under arbitrary-polarization incidences can be completely different as long as $F_+(\boldsymbol{r})|\widehat{\sigma}_+(\boldsymbol{r})\rangle$ is distinct from $F_-(\boldsymbol{r})|\widehat{\sigma}_-(\boldsymbol{r})\rangle$, indicating that we can generate infinite numbers of beams as the incident polarization continuously changes.

Further analyses show that there are two different ways of functionality multiplexing. In the first case where two original beams with opposite helicities are spatially non-overlapping, the scattered field generated under arbitrary-polarization incidence still contains two spatially-separated beams, but with strengths ($|A_{\pm}|^2$) continuously modulated by varying the incident polarization. On the other hand, the case where two original beams are spatially overlapping is more interesting. At every single position $\boldsymbol{r}$, we can always get

$$A_+ \cdot F_+(\boldsymbol{r})|\widehat{\sigma}_+(\boldsymbol{r})\rangle + A_- \cdot F_-(\boldsymbol{r})|\widehat{\sigma}_-(\boldsymbol{r})\rangle$$
$$= F_f(\boldsymbol{r})|\widehat{\sigma}_f(\boldsymbol{r})\rangle \ , \qquad (1)$$

which means that coherent interferences between two scattered beams can generate a new vectorial beam exhibiting a new wave-front (dictated by $F_f(\boldsymbol{r})$) and a new LPD (dictated by $\widehat{\sigma}_f(\boldsymbol{r})$). Obviously, $F_f(\boldsymbol{r})$ and $\widehat{\sigma}_f(\boldsymbol{r})$ sensitively depend on the two complex amplitudes $A_{\pm}$, which in turn, dictated by the incident polarization state.

Before experimentally validating the above two schemes, we first design a series of metaatoms suitable for constructing our metadevices, and experimentally characterize their optical properties. As discussed in previous paragraphs, the desired metaatoms should scatter light with tailored phase and polarization. To achieve this end, we choose the metaatom in metal/insulator/metal (MIM) configuration [Fig. 2(a)] as our building block, where the metallic resonator on the top layer is rotated by an angle ξ with respect to the laboratory system. Suppose that such a metaatom possesses mirror-reflection symmetries against two local axes denoted by

u and v, and exhibits a reflection Jones-Matrix $\boldsymbol{R} = \begin{pmatrix} |r_{uu}|\,\mathrm{e}^{\mathrm{i}\Phi_u} & \\ & |r_{vv}|\,\mathrm{e}^{\mathrm{i}\Phi_v} \end{pmatrix}$ in linear-polarization (LP) bases where $|r_{uu,vv}|$ and $\Phi_{u,v}$ represent reflection amplitudes and phases, respectively. Then, the rotated metaatom must exhibit a Jones-Matrix $\tilde{\boldsymbol{R}} = \boldsymbol{S}\boldsymbol{M}(\xi)\begin{pmatrix} r_{uu} & 0 \\ 0 & r_{vv} \end{pmatrix}\boldsymbol{M}(\xi)^{-1}\boldsymbol{S}^{-1}$ in circular-polarization (CP) bases (with $\begin{pmatrix} 1 \\ 0 \end{pmatrix}$ and $\begin{pmatrix} 0 \\ 1 \end{pmatrix}$ denoting LCP and RCP states, respectively), where $\boldsymbol{M}(\xi) = \begin{pmatrix} \cos\xi & -\sin\xi \\ \sin\xi & \cos\xi \end{pmatrix}$ and $\boldsymbol{S} = \frac{\sqrt{2}}{2}\begin{pmatrix} 1 & -\mathrm{i} \\ 1 & \mathrm{i} \end{pmatrix}$ describe, respectively, the rotation operation and the LP-CP base transformation. We first neglect material losses as we establish the theoretical framework, i.e. suppose that $|r_{uu}| = |r_{vv}| = 1$, $r_{uu} = \mathrm{e}^{\mathrm{i}\Phi_u}$ and $r_{vv} = \mathrm{e}^{\mathrm{i}\Phi_v}$. Under illuminations of CP light with different helicities, through simple derivations we find that the scattered waves can be written as (see Supplementary information (SI) for details):

$$\tilde{\boldsymbol{R}}|\sigma\rangle = \mathrm{e}^{\mathrm{i}\Phi^{\sigma}}\begin{pmatrix} \mathrm{e}^{-\mathrm{i}\Psi^{\sigma}/2}\cos(\Theta^{\sigma}/2) \\ \mathrm{e}^{\mathrm{i}\Psi^{\sigma}/2}\sin(\Theta^{\sigma}/2) \end{pmatrix} \ , \qquad (2)$$

where

$$\begin{cases} \Phi^{\sigma} = \Phi_{\mathrm{Res}} + \Phi_{\mathrm{PB}} \\ \Theta^{\sigma} = \sigma\left(\Delta\Phi - \dfrac{\pi}{2}\right) + \dfrac{\pi}{2} \\ \Psi^{\sigma} = 2\xi - \sigma\dfrac{\pi}{2} \end{cases} \ , \qquad (3)$$

where, $|\sigma\rangle = |\pm\rangle$ denote the incident LCP and RCP components respectively, $\Delta\Phi = \Phi_v - \Phi_u$ is the difference between reflection phases for incident light polarized along two local axes, $\Phi_{\mathrm{Res}} = (\Phi_u + \Phi_v)/2 - \pi/4$ denotes the polarization-independent resonant phase, and $\Phi_{\mathrm{PB}} = \sigma \cdot \xi$ is the polarization-dependent geometric phase which is of the Pancharatnam–Berry (PB) origin[45–50]. Note that in the special case of $\Delta\Phi = \pm\pi$ where degeneracy of polarization states happens, it is customized to re-define these phases as $\Phi^{\sigma} = \Phi_u + \sigma \cdot 2\xi$, $\Theta^{\sigma} = \pi\sigma/2 + \pi/2$ and $\Psi^{\sigma} = 0$, respectively (see ref.[28] for detailed explanations). Equations (2, 3) indicate that, by selecting appropriate MIM metaatoms yielding desired reflection phases $\{\Phi_u, \Phi_v\}$ (or equivalently, $\{\Phi_{\mathrm{Res}}, \Delta\Phi\}$) and rotation angles ξ, we can achieve scattered waves with pre-designed phases (i.e., Φ^{σ}) and polarization states (characterized by $\{\Theta^{\sigma}, \Psi^{\sigma}\}$), as shined by a CP light beam with a particular spin.

We now design a series of MIM metaatoms that are
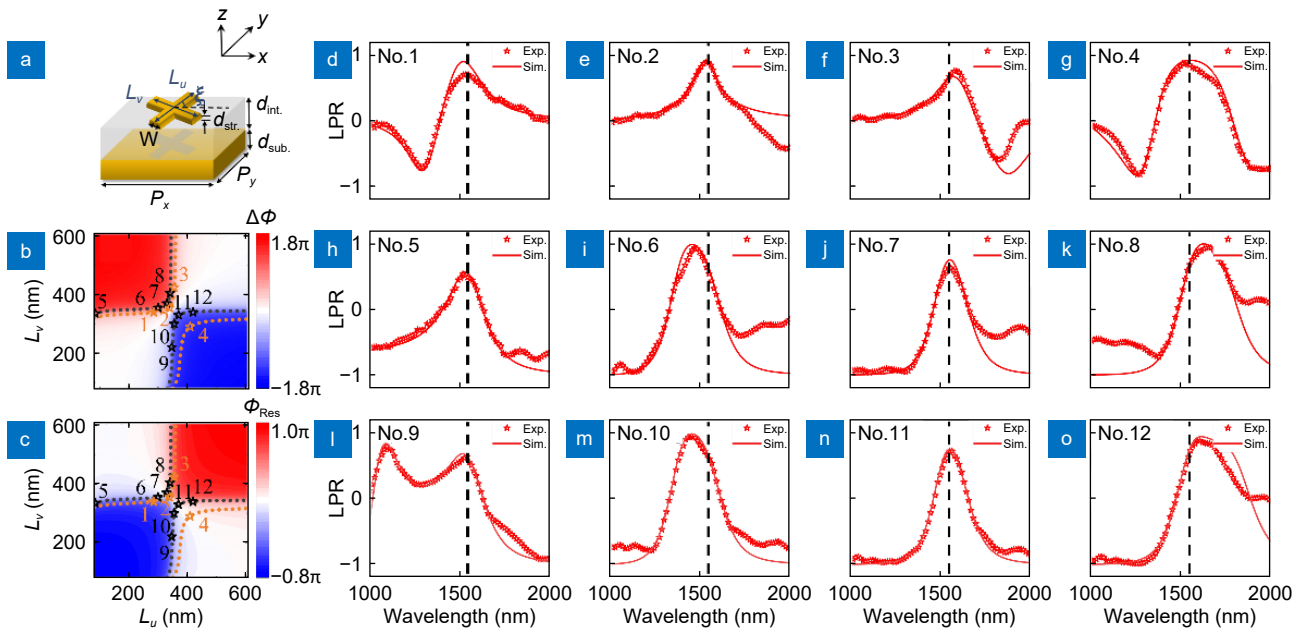
Fig. 2 | Schematic, phase diagrams and experimental characterizations of metaatoms. (**a**) Schematic of the designed metal-insulator-metal meta-atom with geometric parameters $d_{Str} = 30$ nm, $d_{Sub} = 120$ nm, $d_{Int} = 120$ nm, $w = 80$ nm, and $P_x = P_y = 625$ nm fixed. FDTD-simulated (**b**) phase difference $\Delta\Phi$ and (**c**) resonant phase Φ_{Res} of metaatoms with different L_u and L_v at the wavelength of 1550 nm. Orange dashed lines denote the cases $\Delta\Phi = 0.5\pi$ and -1.5π and black dashed lines denote the cases $\Delta\Phi = \pm\pi$. Orange and black stars represent metaatoms labelled as Nos. 1–4 (functioning as QWPs) and Nos. 5–12 (functioning as HWPs), correspondingly. Experimentally measured LPR spectra of metaatoms (**d**) No.1, (**e**) No.2, (**f**) No.3, (**g**) No.4 under the RCP incidence and metaatoms (**h**) No.5, (**i**) No.6, (**j**) No.7, (**k**) No.8, (**l**) No.9, (**m**) No.10, (**n**) No.11, (**o**) No.12 under the incidence of LP light polarized along the angle 135°. Dashed lines denote the positions of 1550 nm.

used later for constructing our metadevices. Since the role of rotation angle ξ is clear, we only focus on choosing MIM metaatoms yielding desired reflection phases $\{\Phi_{Res}, \Delta\Phi\}$. As depicted in Fig. 2(a), our MIM metaatom consists of a 30 nm - thick Au metallic cross formed by two bars with lengths L_u and L_v, a 120 nm - thick continuous Au film, and a 120 nm - thick SiO$_2$ spacer separating two metallic layers. Fixing the widths of all metallic bars as $w = 80$ nm, we employ finite-difference-time-domain (FDTD) simulations to study how the reflection phases $\{\Phi_{Res}, \Delta\Phi\}$ vary against two lengths (L_u, L_v) of the metaatom, which is repeated along u and v directions to form a square lattice with periodicity $P_x = P_y = 625$ nm. Figure 2(b, c) depict the simulated $\Delta\Phi$ and Φ_{Res} as functions of L_u and L_v, indicating that metaatoms with desired $\Delta\Phi$ and Φ_{Res} can be obtained via selecting appropriate L_u and L_v.

Figure 2(b, c) help us efficiently design all metaatoms needed to construct the metadevices realized in this work. As an illustration, we experimentally characterize 12 metaatoms that we designed, with 4 of them (labelled as Nos. 1–4 in Fig. 2(b, c)) functioning as quarter-wave-plates (QWPs) with $\Delta\Phi = \pi/2$ but exhibiting different

resonant phases Φ_{Res} and the remaining 8 metaatoms (labelled as Nos. 5–12 in Fig. 2(b, c)) being half-wave-plates (HWPs) with $\Delta\Phi = \pi$ exhibiting different resonant phases Φ_{Res}. We fabricate 12 realistic samples, each containing a periodic array (with periodicity $P_x = P_y = 625$ nm) of metaatoms with structural parameters L_u and L_v marked in Fig. 2(b, c) (see Section 1 in SI for their geometrical parameters and scanning-electron-microscopy (SEM) images), and measure their reflection spectra using the experimental setup schematically depicted in Fig. S9 of SI. To characterize $\Delta\Phi$, we experimentally measure the linear-polarization rate (LPR) of these samples under different light incidences. Here, LPR is defined as $LPR = \frac{|I_{max} - I_{min}|}{|I_{max} + I_{min}|}$ with I_{max} and I_{min} denoting the maximum and minimum intensities of light reflected by the sample, as a linear polarizer is placed in front of the receiver and rotated to filter out light waves with certain linear polarizations. As shown in Fig. 2(d–g), under the RCP incidence, the measured LPRs of samples 1–4 are close to 1 at the vicinity of 1550 nm (see dashed lines), indicating that these metaatoms are indeed functioning as QWPs with $\Delta\Phi = \pi/2$. We also measure polarization-filtered intensity patterns of light

waves reflected by these samples under the illuminations LCP light at 1550 nm. The measured patterns (see Fig. S5 in SI) clearly show that the reflected light beams are linearly polarized, reinforcing the notion that these metaatoms all function as QWPs. As for samples 5–12, we shine them with LP light beams with E field polarized along the angle of 135° with respect to the u axis and measure their LPR spectra. Figure 2(h−o) show that the measured LPRs of these samples are close to 1 around the wavelength 1550 nm while the polarizations of reflected lights are approximately along the angle of 45° with respect to the u axis (see Fig. S5 in SI), unambiguously demonstrating that these metaatoms behave as HWPs with $\Delta\Phi = \pi$. However, we cannot directly measure Φ_{Res} of these samples due to lacking appropriate experimental setup. Instead, we reply on numerical simulations to characterize the phase responses of these samples. Simulated spectra of reflection phases and Φ_{Res} are depicted in Figs. S3, S4 of SI, showing that these QWPs and HWPs possess different Φ_{Res} in consistency with those given in Fig. 2(c).

With suitable metaatoms designed, we next employ them to construct two functionality-multiplexing metadevices based on two strategies described in this section, and experimentally characterize their wave-manipulation capabilities as they are shined by light beams with continuously varied polarization states.

Metadevice I: A multi-vortex-beam multiplexer

We now construct our first metadevice based on the first strategy, which can generate two distinct vortex beams exhibiting different strengths as the incident polarization changes. Strictly speaking, such a metadevice does not belong to the class of multifunctional metadevices exhibiting infinite functionalities due to coherent interferences. However, we find that studying this metadevice I can vividly illustrate the concept of modulating the intensities of LCP and RCP components inside the incident beam via tuning the polarization state, which is essential for the readers to understand the mechanism proposed in this paper. As discussed in the last section, we need to design a metasurface that can generate two spatially non-overlapping vortex beams carrying different topological charges (l^+ and l^-), as shined by CP light beams with opposite spins. According to these requirements, we design a metasurface exhibiting the following distributions of reflection phase (Φ_{tar}^{σ}) and polarization state (characterized by $\{\Theta_{tar}^{\sigma}, \Psi_{tar}^{\sigma}\}$), as shined by CP light

with spin σ:

$$\begin{cases} \Phi_{tar}^{\sigma}(\boldsymbol{r}) = \zeta_x^{\sigma}x + l^{\sigma}\phi \\ \Theta_{tar}^{\sigma}(\boldsymbol{r}) = \dfrac{\pi}{2}(\sigma + 1) \\ \Psi_{tar}^{\sigma}(\boldsymbol{r}) = 0 \end{cases}, \qquad (4)$$

here, we set $\zeta_x^+ = 5\pi/8P_x$ and $\zeta_x^- = -3\pi/8P_x$ to ensure that different CP components inside the incident light are reflected to opposite sides of the surface normal with angles $\theta_r^+ = \arcsin(\zeta_x^+/k_0) \approx 51°$ and $\theta_r^- = \arcsin(\zeta_x^-/k_0) \approx -28°$, respectively[6–8]. Meanwhile, vortex beams generated under two different CP incidences will carry different topological charges ($l^+ = 3$ and $l^- = -1$), as expected. With these distributions, we then retrieve the required geometrical parameters $\{L_u, L_v, \xi\}$ of metaatoms located at different positions, and fabricate the designed metadevice with its SEM picture and a zoom-in picture shown in Fig. 3(b). We note that all metaatoms needed here are HWPs, though exhibiting different resonant phases.

We experimentally characterize the wave-scattering properties of the fabricated metadevice, starting from considering two extreme cases — the LCP and RCP incidences. Figure 3(d) and 3(h) depict the measured angular distributions of reflected light intensities at different wavelengths under LCP and RCP incidences, respectively. In each case, we find clearly that the normally incident LCP (or RCP) light beam is anomalously reflected to a pre-designed angle at the right-hand (or left-hand) side of the surface normal, as expected. We then employ a home-made Michaelson interferometer to characterize the OAM carried by the reflected beams in these two extreme cases[51,52], at the wavelength of 1550 nm. We interfere the reflected beams with a spherical wave and record the interference patterns in Fig. 3(i) (for LCP incidence) and Fig. 3(m) (for RCP incidence), respectively. The third-order spiral shape and its up-side-down first-order counterpart observed in Fig. 3(i, m) indicate that the generated light beams carry topological charges of $l^+ = +3$ and $l^- = -1$, respectively.

With two extreme cases studied, we next characterize the incident-polarization-dependent wave-scattering properties of the fabricated metadevice. Setting the incident polarization as $|\sigma_0\rangle = \cos\dfrac{\Theta_0}{2}|+\rangle + \sin\dfrac{\Theta_0}{2}|-\rangle$ with Θ_0 continuously varying from 0 to π, we find that the pattern of wave scattered by our metadevice is continuously modulated. Choosing $\Theta_0 = 0, \pi/3, \pi/2, 2\pi/3$ and π as example points labelled as 1, 2, 3, 4, 5 on a specific trajectory on the Poincare's sphere (see inset to Fig. 3(c)),
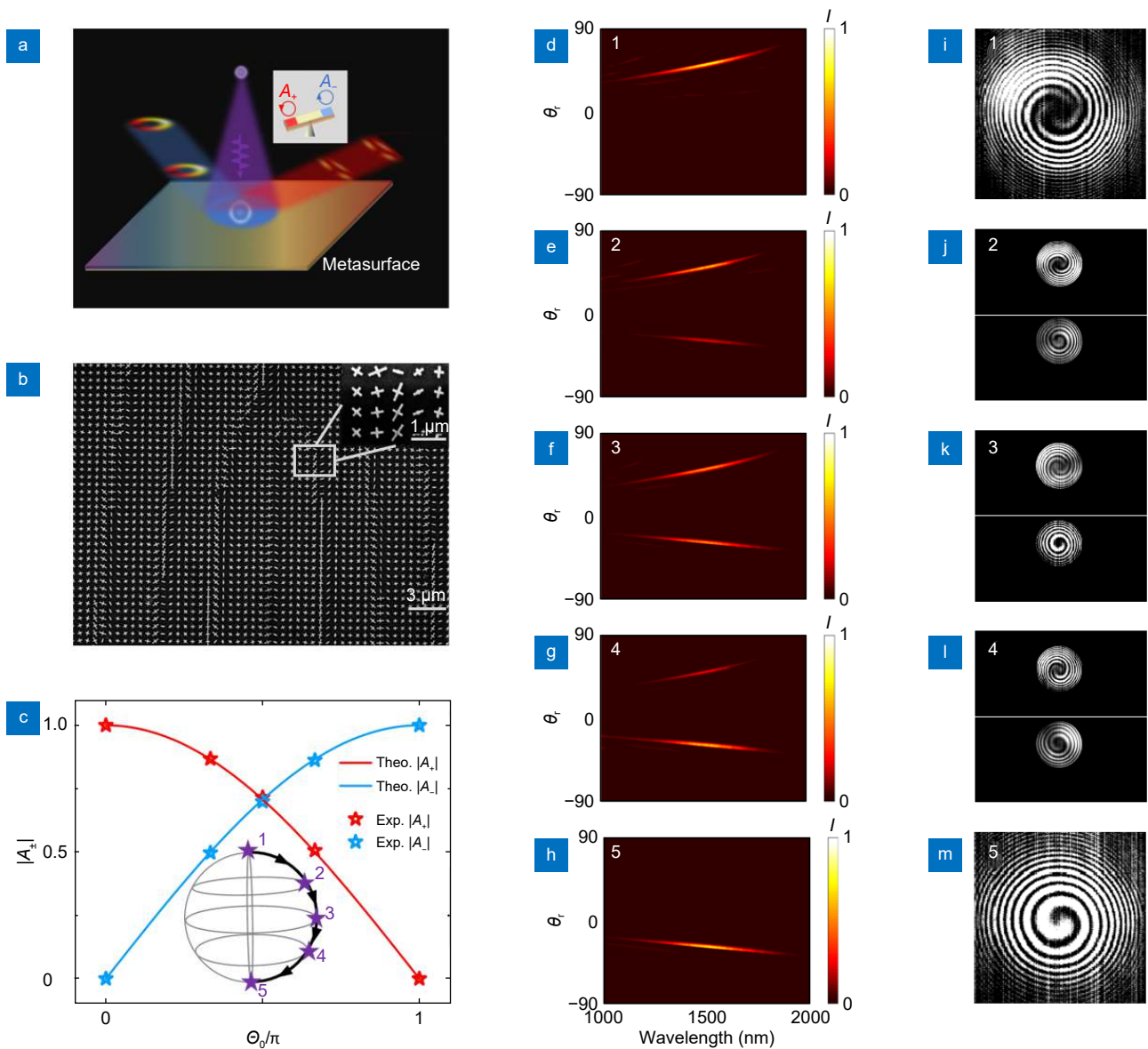
Fig. 3 | Experimental characterizations on metadevice I. (**a**) Schematic illustration of working principle of metadevice I: The device can generate two spatially separating vortex beams carrying different topological charges with strengths tuned by varying the LCP/RCP components inside the incident beam. (**b**) SEM image of the fabricated sample and a zoom-in picture (inset). (**c**) Amplitudes of two beams ($|A_+|$ (red) and $|A_-|$ (blue)) versus Θ_0 obtained from theoretical calculations (line) and experimental measurements (stars); Five polarization states labelled by 1, 2, 3, 4 and 5 on the Poincare's sphere, adopted as incident polarizations for further experimental characterizations. (**d–h**) Experimentally measured angular distributions of intensity of light reflected by our metasurface under illuminations of normally incident light with different wavelengths exhibiting polarizations corresponding to those 5 points on the Poincare's sphere as shown in (c). (**i–m**) Measured interference patterns between a spherical wave and the waves reflected by the metasurface, as shined by normally incident light at 1550 nm with polarizations corresponding to those 5 points on the Poincare' sphere as shown in (c). Only a single interference pattern is shown in (i) and (m) as only one reflected beam exists in these two cases.

we measure the angular distributions of reflected light intensity at different wavelengths, as illustrated in Fig. 3(d–h). In general cases, there are two reflected light beams propagating respectively along the angles of 51° and −28° at the central wavelength of 1550 nm. Meanwhile, the strength of the −28°-directed beam increases

while that of the 51°-directed beam decreases as Θ_0 continuously increases, and the experimentally measured amplitudes $|A_+|$ and $|A_-|$ of two reflection beams at different incident angles are compared with their theoretically calculated counterparts (see solid lines in Fig. 3(c)) to capture the corresponding quantitative

relation between the intensity of the vortex light and the polarization state of the incident light. Excellent agreement between theoretical and experimental results is noted. We next perform similar interference experiments as in the LCP/RCP cases to characterize the OAM properties of the reflected light beams. Interference patterns reveal that the $51°$-directed beam takes an OAM of $l^+ = +3$ while the $-28°$-directed one takes an OAM of $l^- = -1$ [Fig. 3(i–m)], as expected.

Metadevice II: A vectorial-vortex-beam multiplexer

We now construct our second metadevice that can realize a vectorial vortex beam with OAM and LPD continuously tuned by varying the incident polarization. As mentioned in previous sections, we need to first design a metasurface that can generate two vortex beams carrying distinct OAMs and LPDs yet propagating along the *same* direction, as shined by CP light beams with opposite helicities. Following this guideline, we request our metasurface to exhibit the following spin-dependent distributions of reflection phase ($\Phi_{\text{tar}}^{\sigma}$) and polarization state (characterized by $\{\Theta_{\text{tar}}^{\sigma}, \Psi_{\text{tar}}^{\sigma}\}$):

$$\begin{cases} \Phi_{\text{tar}}^{\sigma}(\boldsymbol{r}) = l^{\sigma}\phi \\ \Theta_{\text{tar}}^{\sigma}(\boldsymbol{r}) = \dfrac{\pi}{2}(\sigma+1) \\ \Psi_{\text{tar}}^{\sigma}(\boldsymbol{r}) = 0 \end{cases}, \qquad (5)$$

with $l^+ = 4$ and $l^- = 0$. Different from metadevice I (see Eq. (4)), we note that in this case the two vortex beams generated under LCP and RCP incidences are expected to propagate along the same direction, though exhibiting different OAMs and LPDs. Suppose that the incident polarization is an EP one with $|\boldsymbol{\sigma}_0\rangle = A_+ |+\rangle + A_- |-\rangle$, we find that the reflected light wave can be generally written as $F_f(\boldsymbol{r})|\widehat{\sigma}_f(\boldsymbol{r})\rangle$ $= e^{i\Phi_{\text{tar}}^{\text{EP}}(\boldsymbol{r})} \begin{pmatrix} e^{-i\Psi_{\text{tar}}^{\text{EP}}(\boldsymbol{r})/2}\cos(\Theta_{\text{tar}}^{\text{EP}}(\boldsymbol{r})/2) \\ e^{+i\Psi_{\text{tar}}^{\text{EP}}(\boldsymbol{r})/2}\sin(\Theta_{\text{tar}}^{\text{EP}}(\boldsymbol{r})/2) \end{pmatrix}$, where the involved functions take the following analytical expressions [see derivation details in Section 2.3 in SI]:

$$\begin{cases} \Phi_{\text{tar}}^{\text{EP}}(\boldsymbol{r}) = 2\phi + \dfrac{\arg(A_+)+\arg(A_-)}{2} \\ \Theta_{\text{tar}}^{\text{EP}} = 2\arctan\dfrac{|A_+|}{|A_-|} \\ \Psi_{\text{tar}}^{\text{EP}}(\boldsymbol{r}) = 4\phi + \arg(A_+) - \arg(A_-) \end{cases}, \qquad (6)$$

for the general case with $|A_+| \cdot |A_-| \neq 0$. We note that $\Theta_{\text{tar}}^{\text{EP}}$ is independent of position $\boldsymbol{r}$ and $\Psi_{\text{tar}}^{\text{EP}}$ is a linear function of the azimuthal angle ϕ. Meanwhile, in the special cases of LCP or RCP incidences with $|A_+| \cdot |A_-| = 0$,

Eq. (6) is no longer valid since some terms in Eq. (6) are ill-defined. Under such circumstances, these functions should be rewritten as $\Phi_{\text{tar}}^+(\boldsymbol{r}) = 4\phi$, $\Theta_{\text{tar}}^+ = \pi$, $\Psi_{\text{tar}}^+(\boldsymbol{r}) = 0$ for the case of LCP incidence and $\Phi_{\text{tar}}^-(\boldsymbol{r}) = \Theta_{\text{tar}}^- = \Psi_{\text{tar}}^-(\boldsymbol{r}) = 0$ for the case of RCP incidence.

Expressions given in Eq. (6) capture the essential properties of waves scattered by a metasurface described by Eq. (5), under the illumination of an EP light with A_+ and A_-. Obviously, $\Theta_{\text{tar}}^{\text{EP}}$ and $\Psi_{\text{tar}}^{\text{EP}}(\boldsymbol{r})$ characterize the LPD property of the generated light beam. Meanwhile, in the generic case that the reflected light is a vectorial beam, $\Phi_{\text{tar}}^{\text{EP}}(\boldsymbol{r})$ alone is not enough to dictate the OAM carried by the beam, and the inhomogeneous LPD can also contribute to the OAM[53,54]. Mathematically, as the metasurface is illuminated by an EP light with $|\widehat{\sigma}_{\text{in}}\rangle = A_+ |+\rangle + A_- |-\rangle$, we can derive the field distribution on the *xy*-plane right above the metasurface as $\boldsymbol{E}(\boldsymbol{r}) = \left[e^{-i\Psi_{\text{tar}}^{\text{EP}}(\boldsymbol{r})/2}\cos(\Theta_{\text{tar}}^{\text{EP}}/2)\,\widehat{\boldsymbol{e}}_+ + e^{i\Psi_{\text{tar}}^{\text{EP}}(\boldsymbol{r})/2}\sin(\Theta_{\text{tar}}^{\text{EP}}/2) \right.$ $\left. \widehat{\boldsymbol{e}}_- \right] e^{i\Phi_{\text{tar}}^{\text{EP}}(\boldsymbol{r})} + E_z(\boldsymbol{r})\widehat{\boldsymbol{z}}$, based on Huygens' principle. Under the paraxial approximation, we can derive the time-averaged OAM per unit length of the light beam as $\int \langle l_z(\boldsymbol{r}) \rangle$ $\mathrm{d}^2\boldsymbol{r}_\perp = \int \dfrac{\varepsilon_0}{2\omega}\left(\dfrac{\partial \Phi_{\text{tar}}^{\text{EP}}(\boldsymbol{r})}{\partial \phi} - \dfrac{1}{2}\cos\Theta_{\text{tar}}^{\text{EP}}\dfrac{\partial \Psi_{\text{tar}}^{\text{EP}}(\boldsymbol{r})}{\partial \phi} \right)\mathrm{d}^2\boldsymbol{r}_\perp$. Meanwhile, noting that the time-averaged energy per unit length stored in the light beam is $\int \langle e \rangle \, \mathrm{d}^2\boldsymbol{r}_\perp = \dfrac{\varepsilon_0}{2}\int \mathrm{d}^2\boldsymbol{r}_\perp$, we find that the averaged OAM per photon carried by the light beam is [see derivation details in Section 2.3 in SI]:

$$L_z = \hbar\omega \frac{\int \langle l_z(\boldsymbol{r})\rangle \, \mathrm{d}^2\boldsymbol{r}_\perp}{\int \langle e \rangle \, \mathrm{d}^2\boldsymbol{r}_\perp} = \left[2 - 2\cos\left(2\arctan\frac{|A_+|}{|A_-|} \right) \right]\hbar,$$
$$(7)$$

which sensitively depends on the values of A_+ and A_-. In the extreme cases of $A_+ = 0$ or $A_- = 0$, we get $L_z = 0$ or $L_z = 4$, respectively, in consistency with theoretical expectations. Meanwhile, local polarization at a position $\boldsymbol{r}$ is an EP state with ellipticity γ and orientation angle $\varphi(\boldsymbol{r})$ determined by $\Theta_{\text{tar}}^{\text{EP}}$ and $\Psi_{\text{tar}}^{\text{EP}}(\boldsymbol{r})$ through the following equations,

$$\begin{cases} \gamma = \cos\Theta_{\text{tar}}^{\text{EP}} = \cos\left(2\arctan\dfrac{|A_+|}{|A_-|} \right) \\ \varphi(\boldsymbol{r}) = \dfrac{\Psi_{\text{tar}}^{\text{EP}}(\boldsymbol{r})}{2} = 2\phi + \dfrac{\arg(A_+)-\arg(A_-)}{2} \end{cases}, \qquad (8)$$

for the general case with $|A_+||A_-| \neq 0$. In the special cases of LCP or RCP incidence with $|A_+| \cdot |A_-| = 0$, we

have $\gamma = -1, \varphi = 0$ for the LCP incidence and $\gamma = 1, \varphi = 0$ for the RCP incidence, respectively. Equations (6–8) clearly show that changing the incident polarization can significantly modulate the OAM property [Eq. (7)] and LPD property [Eq. (8)] of the light beam reflected by our metadevice, through varying two complex amplitudes $\{A_+, A_-\}$.

We now fabricate the metadevice constructed by metaatoms possessing appropriate geometrical parameters retrieved from their properties specified in Eq. (5). Figure 4(a) depicts the SEM picture of the fabricated sample. In what follows, choosing two representative

paths on the Poincare's sphere to change the incident polarization, we will analytically study and experimentally characterize how the light beam reflected by our metasurface is modulated by such polarization changes.

The first path we choose follows the meridian on the Poincare's sphere [Fig. 4(b)] where both Θ_0 and Ψ_0 vary correspondingly. To gain an explicit picture on how the polarization evolves on the trajectory, we choose five representative points $\{(\pi/2,0), (\pi/3,0), (0,0), (2\pi/3,\pi)$ and $(\pi,0)\}$ labelled as 1, 2, 3, 4, and 5, respectively (see Fig. 4(b)). Clearly, the incident polarization changes from LP to EP, LCP, EP, and finally to RCP along the
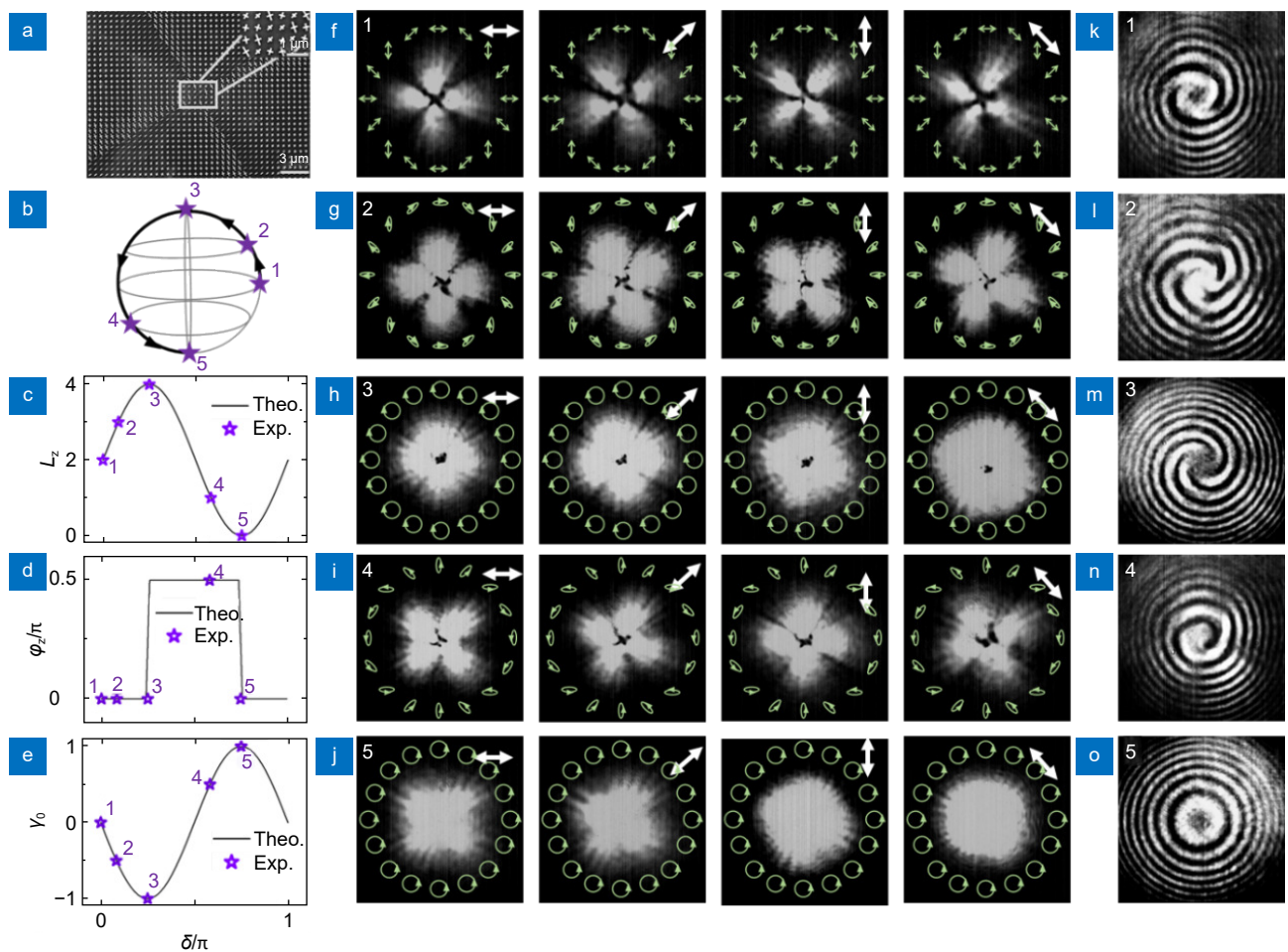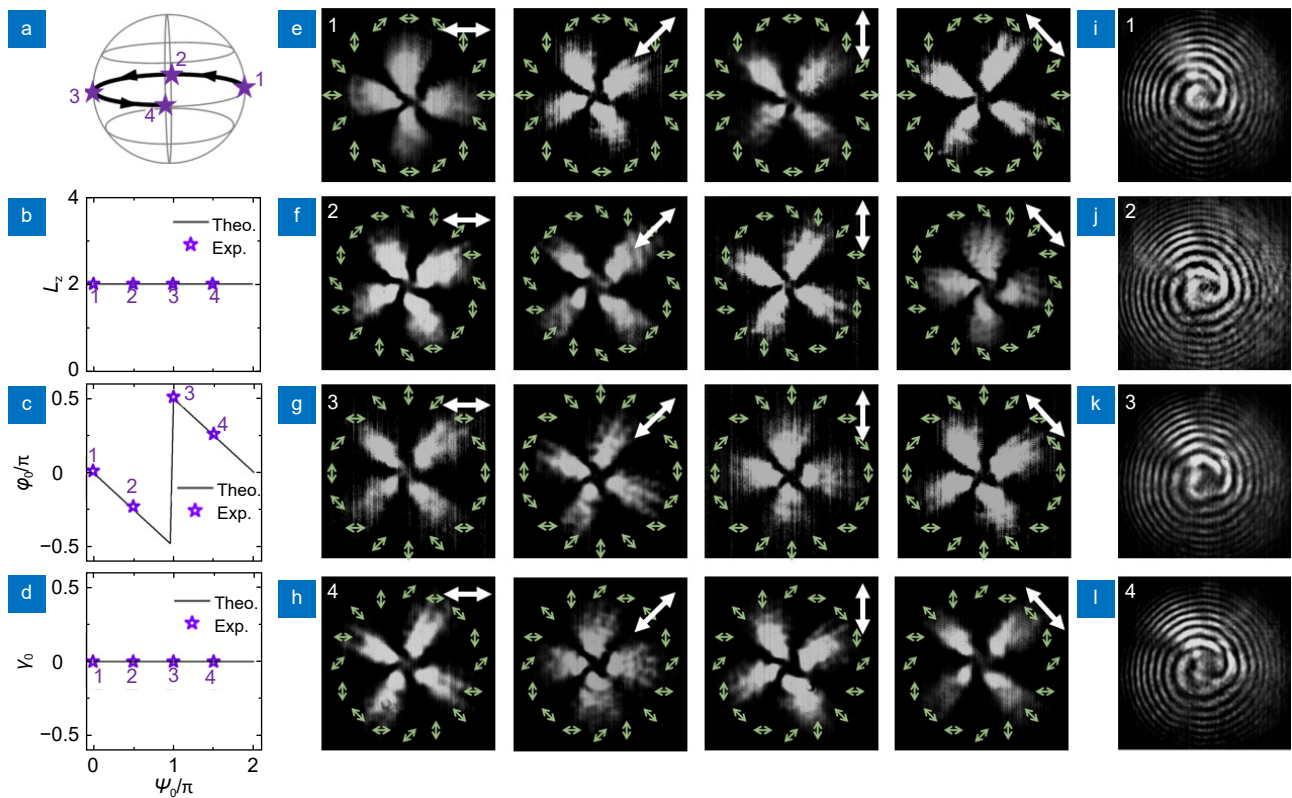

Fig. 4 | Experimental characterizations on metadevice II with incident polarization changing along path-I on the Poincare's sphere. (**a**) SEM image of the fabricated sample and a zoom-in picture (inset). (**b**) Path-I on the Poincare's sphere on which the incident polarization varies, with 1, 2, 3, 4 and 5 denoting five incident polarization states adopted for experimental characterizations. Theoretically calculated (line) and experimentally measured (stars) values of (**c**) L_z (**d**) φ_0 and (**e**) γ_0 versus the parameter δ, which is the relative angle between a linear polarizer and a QWP employed in experiments to generate the desired incident polarization state. Measured intensity patterns of light reflected by our metasurface, under the illuminations of light at 1550 nm with polarizations with number (**f**) 1, (**g**) 2, (**h**) 3, (**i**) 4, and (**j**) 5 on the Poincare's sphere as shown in (b), with a rotatable polarizer placed in front of the detecting CCD tiled at the angles indicated by the white double-head arrows shown in right-up corners of each panels. Green symbols (arrows/circles/ellipse) illustrate the theoretically predicted polarization distributions in different cases. (**k-o**) Measured interference patterns between a spherical wave and the waves reflected by the metasurface, as shined by normally incident light at 1550 nm with polarizations corresponding to those 5 points on the Poincare' sphere as shown in (b).

trajectory, with $\{A_+, A_-\}$ varying correspondingly. To facilitate further analyses, we use $\Theta_0 = 2\arcsin\left|\sqrt{2}(1+i)\right.$ $\left.(e^{2i\delta}-i)/4\right|$ and $\Psi_0 = \arg\left[\sqrt{2}(1+i)(e^{2i\delta}-i)/4\right] - \arg\left\{\sqrt{2}\left[(1+i)+(1-i)e^{2i\delta}\right]/4\right\}$ to describe such a path, where δ is just the relative angle between the linear polarizer and QWP employed in our experiments to generate the desired incident polarization state (see Section 3 in SI). In the special cases of $\delta = \pi/4$ or $3\pi/4$ yielding $\Theta_0 = 0$ or π, we find that Ψ_0 is ill-defined so that we just set $\Psi_0 = 0$. Based on these analytical expressions, we can easily retrieve how $\{A_+, A_-\}$ vary against δ on the path, and then substitute $\{A_+, A_-\}$ into Eqs. (7, 8) to evaluate how the essential properties (i.e. $\{L_z, \gamma, \varphi(\boldsymbol{r})\}$) of reflected light change as the function of δ. As shown by the solid line in Fig. 4(c), OAM carried by each photon in the generated beam changes significantly as a function of δ. This is quite understandable as δ dictates the values of $\{A_+, A_-\}$, which in turn, determine L_z through Eq. (7). Meanwhile, LPD of the reflected beam also changes significantly along with tuning the incident polarization. First of all, we note that LPDs of reflected light beams in these cases all share a common characteristic: Polarization states at different local points exhibit identical ellipticity (i.e., $\gamma \equiv \gamma_0$) and distinct polarization angle. Noticing that the variation of polarization angle φ over the entire 2π range of azimuthal angle ϕ is always 4π, we choose $\varphi_0 = \varphi(\phi=0)$ as a characteristic value to quantitatively describe the change of polarization distribution. Solid lines in Fig. 4(d) and 4(e) depict, respectively, how the theoretically computed γ_0 and φ_0 of the reflected light beam change as varying δ. To gain a pictorial understanding on such changes, we show in Fig. 4(f–j) the expected LPDs of light beams under five selected incident polarizations by double-head green arrows or circles/ellipses.

We perform experiments to verify these theoretical predictions. In our experiments, we employ a QWP combined with a linear polarizer rotated by a relative angle δ to generate the light beam with desired polarization state. Choosing δ appropriately to generate incident light beams with polarizations corresponding to points 1, 2, 3, 4 and 5 on the Poincare's sphere [Fig. 4(b)], we shine the metadevice by the generated light beams and experimentally characterize the properties of reflected light beams. A rotatable polarizer (denoted as the detecting polarizer) is placed in front of the charged couple device (CCD) to analyse the LPDs of reflected beams[27,28].

Figure 4(f–j) depict the CCD-recorded field patterns with the detecting polarizer orientated at different angles (see white arrows), for incident light taking polarizations labelled as 1, 2, 3, 4 and 5, correspondingly. In general, these polarizer-filtered patterns are well consistent with the predicted polarization patterns. For example, under the LP incidence (Fig. 4(f)), four intensity zeros appear in the measured patterns with zero-intensity angles rotating along with the detecting polarizer, implying that the local polarization must be an LP one with polarization direction rotated against the azimuthal angle ϕ. Meanwhile, as the incident polarization becomes an EP state (Fig. 4(g) and 4(i)), no intensity zeros appear in the measured patterns but the measured light intensity still varies against with ϕ, implying that now the local polarization must be an EP state with the polarization angle rotated as a function of ϕ. Finally, under the LCP (Fig. 4(h)) or RCP (Fig. 4(j)) incidence, measured light intensity does not change obviously in all patterns measured, clearly demonstrating that the polarization state at every local point must be a CP one. We retrieve two characteristic quantities $\{\gamma_0, \varphi_0\}$ from the measured patterns under five different incident polarizations (see SI for details) and draw them as stars in Fig. 4(d, e). Experimental values agree well with theoretical predictions (Fig. 4(d, e)). We further employ our home-made Michaelson-interferometer to characterize the OAM properties of the reflected beams under different incident polarizations. Interfering the reflected light beams with a reference spherical wave, we show the obtained interference patterns in Fig. 4(k–o) for incident polarizations 1–5, respectively. Counting the number of bifurcations in these interference patterns, we find that the reflected light beams carry OAMs with topological charges $L_z = +2, +3, +4, +1$ and 0, respectively, in good consistency with theoretical predictions [Fig. 4(c)].

We now consider the second path along the equator on the Poincare's sphere with Θ_0 fixed at $\pi/2$ and Ψ_0 varied continuously (see the bolded line in Fig. 5(a)). On this path the incident polarization is kept as LP but with the orientation angle continuously changed. We retrieve how the two amplitudes $\{A_+, A_-\}$ vary against Ψ_0 on the path, and put them into Eqs. (7, 8) to calculate the essential properties of reflected light beams with different Ψ_0. Theoretical calculations reveal that whereas the OAM carried by the reflected light remains unchanged when the incident polarization varies along the path (see

Fig. 5 | Experimental characterizations on metadevice II with incident polarization changing along path-II on the Poincare's sphere. (**a**) Path-II on the Poincare's sphere on which the incident polarization varies, with 1, 2, 3, and 4 denoting four representative incident polarization states adopted for experimental characterizations. Theoretically calculated (line) and experimentally measured (stars) values of (**b**) L_z (**c**) φ_0 and (**d**) γ_0 versus the parameter Ψ_0, which is the azimuthal angle on the Poincare's sphere. Measured intensity patterns of light reflected by our meta-surface, under the illuminations of light at 1550 nm with polarizations denoted by number (**e**) 1, (**f**) 2, (**g**) 3 and (**h**) 4 on the Poincare's sphere as shown in (a), with a rotatable polarizer placed in front of the detecting CCD tiled at the angles indicated by the white double-head arrows shown in right-up corners of each panels. Green symbols (arrows/circles/ellipse) illustrate the theoretically predicted polarization distributions in different cases. (**i-l**) Measured interference patterns between a spherical wave and the waves reflected by the metasurface, as shined by normally incident light at 1550 nm with polarizations corresponding to those four points on the Poincare' sphere as shown in (a).

Fig. 5(b)), the LPD of the reflected light beam does change significantly. Specifically, we find that the LPDs are all LP ones at each local point (i.e., $\gamma(\mathbf{r}) \equiv 0$, see Fig. 5(d)), but the distribution of polarization angles $\varphi(\mathbf{r})$ changes dramatically as the incident polarization varies. For explicit illustrations, we choose four representative points on the path (labelled as 1, 2, 3, and 4 with Ψ_0 being 0, $\pi/2$, π and $3\pi/2$, respectively), and show in Fig. 5(e–h) the calculated LPDs in different cases by double-head green arrows. Similar to Fig. 4, we use γ_0 and φ_0 to quantitatively characterize the LPD. Figure 5(c, d) depict the calculated γ_0 and φ_0 as functions of Ψ_0, which clearly illustrate how the LPD of the reflected beam changes as varying the incident polarization along the given path on the Poincare's sphere.

We now experimentally verify the above theoretical predictions. In our experiment, we fix the incident polar-

ization as those 4 states specified on the Poincare's sphere, and study the properties of the reflected light beams correspondingly. We employ the same techniques as in Fig. 4 to analyse LPDs of the reflected light beams under four different incident polarizations. The CCD-recorded field patterns with different detection-polarizer orientations are shown in Fig. 5(e–h), for incident light beams carrying polarizations labelled as 1, 2, 3 and 4, respectively. Under a particular incident polarization, measured patterns always contain four intensity zeros with angle positions rotating along with the polarizer orientation, unambiguously illustrating the vectorial nature of the reflected beam. The angular positions of these intensity zeros also consist well with theoretically predicted LPDs. Meanwhile, we find that the intensity zeros obtained under the same detection polarizer also change as the incident polarization varies, reinforcing our

prediction that the LPD of the generated vectorial beam is modulated by varying the incident polarization. We retrieve the values of two characteristic quantities $\{\gamma_0, \varphi_0\}$ from our serial measurements for each incident polarization, and depict them by solid stars in Fig. 5(c, d). Experimental results are in excellent agreement with theoretical predictions. We finally employ our home-made Michaelson-interferometer to characterize the OAM properties of the generated light beams. Interfering the reflected light beams with a spherical wave, we find that the interference patterns (see Fig. 5(i–l)) all indicate that the light beams carry a +2 topological charge, independent of the orientation of incident polarization. This is again in excellent agreement with theoretical predictions [Fig. 5(b)].

Conclusions

In short, we experimentally demonstrate that metadevices exhibiting infinite wave-control functionalities can be realized, based on coherent wave interferences tuned by continuously varying the incident polarization. We first design a series of metaatoms and experimentally demonstrate that they exhibit tailored reflection phases and polarization-conversion capabilities. We next use these metaatoms to construct two functional metadevices exhibiting continuously tuned wave-control functionalities as the incident polarization is modulated along a certain path on the Poincare's sphere. Our experiments reveal that the first metadevice can generate two distinct vortex beams that are non-overlapping in space, with beam strengths continuously tuned by varying the incident polarization. Meanwhile, the second metadevice can generate a single vectorial vortex beam carrying OAM and/or LPD continuously tuned by varying the incident polarization along two specific paths on the Poincare's sphere. Experimental results are in excellent agreement with theoretical predictions. Our findings can find numerous applications in practice and can stimulate many future studies. For example, extensions to near-field and far-field complexing and/or transmissive systems are interesting future projects, and using vectorial beams as the incident light can further enrich the wave-manipulation functionalities of the metadevices.

Materials and methods

Numerical simulation

FDTD simulations are performed using a numerical soft-ware. The permittivity of Au was described by the Drude model $\varepsilon_r(\omega) = \varepsilon_\infty - \dfrac{\omega_p{}^2}{\omega(\omega + \mathrm{i}\Gamma)}$, with $\varepsilon_\infty = 9$, $\omega_p = 1.367 \times 10^{16}\ \mathrm{s}^{-1}$, $\Gamma = 3.1824 \times 10^{14}\ \mathrm{s}^{-1}$, obtained by fitting with experimental results. The SiO$_2$ spacer was considered as a lossless dielectric with permittivity $\varepsilon = 2.25$. Additional losses caused by surface roughness and grain boundary effects in thin films as well as dielectric losses were effectively considered in the fitting parameter Γ. Absorbing boundary conditions were implemented to remove the energy of those scattered waves flowing outside the simulation domain.

Sample fabrication

All MIM tri-layer samples were fabricated using standard thin-film deposition and electron-beam lithography (EBL) techniques. We first deposited 5 nm Cr, 120 nm Au, 5 nm Cr and a 120 nm SiO$_2$ dielectric layer onto a silicon substrate using magnetron DC sputtering (Cr and Au) and RF sputtering (SiO$_2$). Secondly, we lithographed the cross structures with EBL, employing an ~100 nm thick PMMA2 layer at an acceleration voltage of 100 keV. After development in a solution of methyl isobutyl ketone and isopropyl alcohol, a 5 nm Cr adhesion layer and a 30 nm Au layer were subsequently deposited using electron-beam evaporation. The Au patterns were finally formed on top of the SiO$_2$ film after a lift-off process using acetone.

Experimental setup

A homemade near-infra-red (NIR) macroscopic angular resolution spectroscope was employed for characterizations of metadevice I. The size of the incident light spot was minimized to 130 μm. While the sample was placed on a fixed stage, the fibre-coupled receiver equipped with a polarizer was placed on a motorized rotation stage to collect the reflected signal in the right direction. An NIR microimaging system with a homemade Michelson interferometer was employed for characterizations of metadevice II, by performing real-time imaging of the far-field vectorial light beam and its interferences with the reference light.

References

1. Yu NF, Aieta F, Genevet P et al. A broadband, background-free quarter-wave plate based on plasmonic metasurfaces. *Nano Lett* **12**, 6328–6333 (2012).
2. Hao JM, Yuan Y, Ran LX et al. Manipulating electromagnetic wave polarizations by anisotropic metamaterials. *Phys Rev Lett* **99**, 063908 (2007).

3. Mueller JPB, Rubin NA, Devlin RC et al. Metasurface polarization optics: independent phase control of arbitrary orthogonal states of polarization. *Phys Rev Lett* **118**, 113901 (2017).

4. Wang S, Wen S, Deng ZL et al. Metasurface-based solid poincaré sphere polarizer. *Phys Rev Lett* **130**, 123801 (2023).

5. Wang JJ, Li PS, Zhao XQ et al. Optical bound states in the continuum in periodic structures: Mechanisms, effects, and applications. *Photonics Insights* **3**, R01 (2024).

6. Yu NF, Genevet P, Kats MA et al. Light propagation with phase discontinuities: generalized laws of reflection and refraction. *Science* **334**, 333–337 (2011).

7. Sun SL, Yang KY, Wang CM et al. High-efficiency broadband anomalous reflection by gradient meta-surfaces. *Nano Lett* **12**, 6223–6229 (2012).

8. Fang ZN, Li HP, Chen Y et al. Deterministic approach to design passive anomalous-diffraction metasurfaces with nearly 100% efficiency. *Nanophotonics* **12**, 2383–2396 (2023).

9. Xu HX, Ma SJ, Ling XH et al. Deterministic approach to achieve broadband polarization-independent diffusive scatterings based on metasurfaces. *ACS Photonics* **5**, 1691–1702 (2018).

10. Ma Q, Liu C, Xiao Q et al. Information metasurfaces and intelligent metasurfaces. *Photonics Insights* **1**, R01 (2022).

11. Zhang F, Pu MB, Li X et al. All-dielectric metasurfaces for simultaneous giant circular asymmetric transmission and wavefront shaping based on asymmetric photonic spin–orbit interactions. *Adv Funct Mater* **27**, 1704295 (2017).

12. Sun SL, He Q, Xiao SY et al. Gradient-index meta-surfaces as a bridge linking propagating waves and surface waves. *Nat Mater* **11**, 426–431 (2012).

13. Tcvetkova SN, Kwon DH, Díaz-Rubio A et al. Near-perfect conversion of a propagating plane wave into a surface wave using metasurfaces. *Phys Rev B* **97**, 115447 (2018).

14. Cai T, Tang SW, Wang GM et al. High‐performance bifunctional metasurfaces in transmission and reflection geometries. *Adv Opt Mater* **5**, 1600506 (2017).

15. Xu Q, Lang YH, Jiang XH et al. Meta-optics inspired surface plasmon devices. *Photonics Insights* **2**, R02 (2023).

16. Aieta F, Genevet P, Kats MA et al. Aberration-free ultrathin flat lenses and axicons at telecom wavelengths based on plasmonic metasurfaces. *Nano Lett* **12**, 4932–4936 (2012).

17. Arbabi A, Horie Y, Ball AJ et al. Subwavelength-thick lenses with high numerical apertures and large efficiency based on high-contrast transmitarrays. *Nat Commun* **6**, 7069 (2015).

18. Liu FF, Wang DY, Zhu H et al. High‐efficiency metasurface‐based surface‐plasmon lenses. *Laser Photonics Rev* **17**, 2201001 (2023).

19. Wang SM, Wu PC, Su VC et al. A broadband achromatic metalens in the visible. *Nat Nanotechnol* **13**, 227–232 (2018).

20. Xu BB, Li HM, Gao SL et al. Metalens-integrated compact imaging devices for wide-field microscopy. *Adv Photonics* **2**, 066004 (2020).

21. Arbabi A, Horie Y, Bagheri M et al. Dielectric metasurfaces for complete control of phase and polarization with subwavelength spatial resolution and high transmission. *Nat Nanotechnol* **10**, 937–943 (2015).

22. Chen WT, Yang KY, Wang CM et al. High-efficiency broadband meta-hologram with polarization-controlled dual images. *Nano Lett* **14**, 225–230 (2014).

23. Zheng GX, Mühlenbernd H, Kenney M et al. Metasurface holograms reaching 80% efficiency. *Nat Nanotechnol* **10**, 308–312

(2015).

24. Guo XY, Li P, Zhong JZ et al. Stokes meta-hologram toward optical cryptography. *Nat Commun* **13**, 6687 (2022).

25. Yang ZJ, Huang PS, Lin YT et al. Asymmetric full-color vectorial meta-holograms empowered by pairs of exceptional points. *Nano Lett* **24**, 844–851 (2024).

26. Zhang F, Guo YH, Pu MB et al. Meta-optics empowered vector visual cryptography for high security and rapid decryption. *Nat Commun* **14**, 1946 (2023).

27. Wang DY, Liu T, Zhou YJ et al. High-efficiency metadevices for bifunctional generations of vectorial optical fields. *Nanophotonics* **10**, 685–695 (2020).

28. Wang DY, Liu FF, Liu T et al. Efficient generation of complex vectorial optical fields with metasurfaces. *Light Sci Appl* **10**, 67 (2021).

29. Ding F, Chen YT, Yang YQ, et al. Multifunctional metamirrors for broadband focused vector‐beam generation. *Adv Opt Mater* **7**, 1900724 (2019).

30. Liu ZX, Liu YY, Ke YG et al. Generation of arbitrary vector vortex beams on hybrid-order poincaré sphere. *Photonics Res* **5**, 15–21 (2017).

31. Li H, Duan SX, Zheng CL et al. Longitudinal manipulation of scalar to vector vortex beams evolution empowered by all‐silicon metasurfaces. *Adv Opt Mater* **11**, 2301368 (2023).

32. Yue FY, Wen DD, Xin JT et al. Vector vortex beam generation with a single plasmonic metasurface. *ACS Photonics* **3**, 1558–1563 (2016).

33. Cui GS, Gu MN, Cheng C et al. Multifunctional all-dielectric quarter-wave plate metasurfaces for generating focused vector beams of bell-like states. *Nanophotonics* **13**, 1631–1644 (2024).

34. Li X, Chen LW, Li Y et al. Multicolor 3D meta-holography by broadband plasmonic modulation. *Sci Adv* **2**, e1601102 (2016).

35. Li X, Chen QM, Zhang X et al. Time-sequential color code division multiplexing holographic display with metasurface. *Opto-Electron Adv* **6**, 220060 (2023).

36. Shi ZJ, Zhu AY, Li ZY et al. Continuous angle-tunable birefringence with freeform metasurfaces for arbitrary polarization conversion. *Sci Adv* **6**, eaba3367 (2020).

37. Zhang F, Xie X, Pu MB et al. Multistate switching of photonic angular momentum coupling in phase‐change metadevices. *Adv Mater* **32**, 1908194 (2020).

38. Liu YC, Xu K, Fan XH et al. Dynamic interactive bitwise meta-holography with ultra-high computational and display frame rates. *Opto-Electron Adv* **7**, 230108 (2024).

39. Chen J, Wang DP, Si GY et al. Planar peristrophic multiplexing metasurfaces. *Opto-Electron Adv* **6**, 220141 (2023).

40. Xu HX, Tang SW, Ling XH et al. Flexible control of highly-directive emissions based on bifunctional metasurfaces with low polarization cross-talking. *Ann Phys* **529**, 1700045 (2017).

41. Yang WX, Chen K, Luo XY et al. Polarization-selective bifunctional metasurface for high-efficiency millimeter-wave folded transmitarray antenna with circular polarization. *IEEE Trans Antennas Propag* **70**, 8184–8194 (2022).

42. Ding F, Deshpande R, Bozhevolnyi SI. Bifunctional gap-plasmon metasurfaces for visible light: Polarization-controlled unidirectional surface plasmon excitation and beam steering at normal incidence. *Light Sci Appl* **7**, 17178 (2018).

43. Cai XD, Tang R, Zhou HY et al. Dynamically controlling terahertz wavefronts with cascaded metasurfaces. *Adv Photonics* **3**, 036003 (2021).

44. Zhang Q, He ZH, Xie ZW et al. Diffractive optical elements 75 years on: from micro-optics to metasurfaces. *Photonics Insights* **2**, R09 (2023).

45. Xu Q, Su XQ, Zhang XQ et al. Mechanically reprogrammable pancharatnam-berry metasurface for microwaves. *Adv Photonics* **4**, 016002 (2022).

46. Luo WJ, Sun SL, Xu HX et al. Transmissive ultrathin pancharatnam-berry metasurfaces with nearly 100% efficiency. *Phys Rev Appl* **7**, 044033 (2017).

47. Xie X, Pu MB, Jin JJ et al. Generalized pancharatnam-berry phase in rotationally symmetric meta-atoms. *Phys Rev Lett* **126**, 183902 (2021).

48. Cong LQ, Xu NN, Han JG et al. A tunable dispersion‐free terahertz metadevice with pancharatnam–berry‐phase‐enabled modulation and polarization control. *Adv Mater* **27**, 6630–6636 (2015).

49. Ye WM, Zeuner F, Li X et al. Spin and wavelength multiplexed nonlinear metasurface holography. *Nat Commun* **7**, 11930 (2016).

50. Guo YH, Pu MB, Zhang F et al. Classical and generalized geometric phase in electromagnetic metasurfaces. *Photonics Insights* **1**, R03 (2022).

51. Yang YM, Wang WY, Moitra P et al. Dielectric meta-reflectarray for broadband linear polarization conversion and optical vortex generation. *Nano Lett* **14**, 1394–1399 (2014).

52. Liu YF, Zhou L, Wen YZ et al. Optical vector vortex generation by spherulites with cylindrical anisotropy. *Nano Lett* **22**, 2444–2449 (2022).

53. Ling XH, Luo HL, Guan FX et al. Vortex generation in the spin-orbit interaction of a light beam propagating inside a uniaxial medium: origin and efficiency. *Opt Express* **28**, 27258–27267 (2020).

54. Ling XH, Guan FX, Cai XD et al. Topology‐induced phase transitions in spin‐orbit photonics. *Laser Photonics Rev* **15**, 2000492 (2021).

Acknowledgements

Author contributions

Y. J. Zhou fabricated all samples and carried out experimental testing. T. Liu performed all theoretical derivations and design of multiplexing devices. C. H. Dai helped with experimental setup and testing. D. Y. Wang and L. Zhou conceived the idea and supervised the project. All authors contributed to the discussion and preparation of the manuscript.

Competing interests

The authors declare no competing financial interests.

Scan for Article PDF